

## Degradation-Safety Analytics in Lithium-Ion Cells: Part I. Aging under Charge/Discharge Cycling

To cite this article: Daniel Juarez-Robles *et al* 2020 *J. Electrochem. Soc.* **167** 160510

View the [article online](#) for updates and enhancements.

## 239th ECS Meeting

with the 18th International Meeting on Chemical Sensors (IMCS)

**ABSTRACT DEADLINE: DECEMBER 4, 2020**



May 30-June 3, 2021

**SUBMIT NOW →**



# Degradation-Safety Analytics in Lithium-Ion Cells: Part I. Aging under Charge/Discharge Cycling

Daniel Juarez-Robles,<sup>1,2,\*</sup>  Judith A. Jeevarajan,<sup>2,\*</sup>  and Partha P. Mukherjee<sup>1,\*</sup> 

<sup>1</sup>School of Mechanical Engineering, Purdue University, West Lafayette, Indiana 47907, United States of America

<sup>2</sup>Electrochemical Safety, Underwriters Laboratories Inc., Northbrook, Illinois 60062, United States of America

Disparate degradation modes in lithium-ion cell components due to aging under continuous cycling cause capacity fade and safety concerns under abuse conditions. In this work, the interplay between aging and abuse conditions, namely overcharge and external short, is investigated in fresh and aged cylindrical lithium-ion cells for different degradation conditions and operating windows. The objective, to elicit insights into the potential hazards in an aged cell, is accomplished via a comprehensive and controlled experimental analytics of the electrochemical, thermal and morphological behavior of the cell components. The Part I of the study sets the baseline for the aging induced degradation. According to the results of the aging study, cycle life can be doubled by reducing 200 mV at either ends of the voltage window at the expense of having a 20% reduction in capacity utilization. Differential voltage and temperature analyses revealed a state-of-charge dependence of the internal resistance and heat generation rate. Post-mortem analyses showed that the loss of cyclable lithium inventory due to the solid electrolyte interphase (SEI) formation; and electrochemical deactivation of the cathode owing to delamination and particle cracking, are the primary degradation mechanisms responsible for the cell capacity fade due to aging under continuous cycling.

© 2020 The Electrochemical Society ("ECS"). Published on behalf of ECS by IOP Publishing Limited. [DOI: 10.1149/1945-7111/abc8c0]

Manuscript submitted August 23, 2020; revised manuscript received October 16, 2020. Published November 26, 2020.

The success of portable electronics, wireless tools, and electric vehicles depends largely on their energy storage system.<sup>1</sup> Among all the electrochemical energy storage devices, lithium-ion batteries (LIBs) currently have the best properties to fulfill the wide range of requirements specific for these applications—high energy density, long lifetime, good power capabilities and also relatively low cost.<sup>2,3</sup> The most beneficial combination of all these properties is the one which results in a cell with light weight, small volume, high voltage and high capacity.<sup>4</sup> Regardless of their superior performance over other energy storage systems, LIBs are still perceived as a threat mainly due to their reactive, flammable and volatile components.<sup>5,6</sup>

**Safety.**—In recent years, safety issues associated with LIBs have been in the eye of the storm, mostly due to highly publicized events where Li-ion cells catching fire were involved.<sup>7</sup> In 2010, the Boeing 747 cargo plane, departing as UPS Airlines Flight 6, crashed due to the autoignition of a lithium-ion cells cargo pallet.<sup>8</sup> According to the FAA, to date, there had been 206 airport incidents involving lithium batteries since March 1991.<sup>9</sup> Safety concerns become more significant when they involve devices used in daily life. In September 2016, Samsung was forced to recall nearly 1 million Galaxy Note 7 phones after numerous reports of the devices going into thermal runaway during charging or use.<sup>10</sup> It was later revealed that the issue stemmed from two independent cell design flaws by the two different manufacturers, causing them to short circuit internally. In February 2017, a Dell Inspiron laptop powered by a LIB violently combusted while charging and proceeded to burst into flames three more times after being unplugged.<sup>11</sup> These examples illuminate the propensity of the Li-ion chemistry to go into a catastrophic failure mode and demonstrate the necessity of understanding the response of Li-ion cells to abnormal conditions.<sup>12,13</sup>

**LIBs and degradation mechanisms.**—Li-ion cells are a member of the secondary (rechargeable) battery type in which lithium ions have the ability to move from anode to cathode and vice versa depending on the discharge or charge process, respectively. In order to obtain a reversible electrochemical system, intercalation/deintercalation reactions occur. Intercalation/deintercalation reactions involve the reversible insertion and extraction of a Li-ion into the

anode with minimal alterations to the host crystal,<sup>14</sup> while the electrolyte serves as the transportation medium for the lithium ions. To preserve electrical neutrality, during the charging process, Li-ions move from the cathode and eventually intercalates in the anode. As a consequence of the electrochemical processes, slight changes (degradation) on the electrode microstructure and composition are induced in a progressive and unpredictable way. The capacity reduction of the cell associated with those changes is an intrinsic degradation mechanism that cannot be avoided but can be partially controlled based on the storage<sup>15</sup> (calendar) and cycling (aging) conditions.<sup>16,17</sup>

**Calendar aging.**—Calendar life refers to all aging processes leading to degradation of Li-ion cells independently of the charge/discharge history.<sup>18,19</sup> In contrast to the cycling life, where mechanical strain in the electrode active materials<sup>20</sup> or lithium plating<sup>21,22</sup> can cause severe degradation, the predominant mechanism of calendar aging is the evolution of passivating layers at the electrode–electrolyte interfaces. The formation, growth, or reconstruction of passivation layers consumes cyclable lithium ions as a result of electrolyte decomposition, i.e., reduction at the anode and oxidation at the cathode interface.<sup>23</sup> Furthermore, the growth of the passivation layer at the anode, which is usually referred to as the Solid Electrolyte Interphase (SEI), is said to be additionally catalyzed by dissolved transition-metal ions from the cathode, which are in turn reduced again to metals at the anode.<sup>24,25</sup> State of Charge (SOC),<sup>26</sup> storage temperature, and the length of the storage time are the main factors driving the calendar aging degradation. Grolleau et al. found that the storage temperature has a stronger impact on the degradation rate and it aggravates if cells are stored at higher SOC.<sup>27</sup>

**Cycle life aging.**—Aging due to cycle life refers to all the degradation processes associated with the charge and discharge processes. Every time a Li-ion cell is cycled, its capacity reduces mostly in an imperceptible way. However, in the long-term cycling, the cell loses a significant amount of its initial capacity.<sup>15</sup> The rate of capacity loss depends upon multiple factors like operating temperature,<sup>17,28–30</sup> cycling protocol,<sup>31</sup> C-rate,<sup>32</sup> and the charge/discharge cut-off voltages.<sup>33,34</sup> Determining the actual state of health of the cells after cycling is essential for recycling or repurposing them in secondary-use applications.<sup>35,36</sup>

Waldmann et al. studied the aging behavior of graphite/NMC + LMO cells in the operating temperature range of  $-20$  °C to  $70$  °C. Cells exhibited a minimum degradation rate at  $25$  °C and it aggravated for higher and lower operating temperatures.<sup>30</sup> At low

\*Electrochemical Society Member.

<sup>z</sup>E-mail: Judy.Jeevarajan@ul.org; pmukherjee@purdue.edu

temperatures, aging is dominated by lithium plating, whereas, at high temperatures aging is dominated by cathode active material degradation, electrolyte decomposition and a repeated passivating layer growth on the anode.<sup>28,37</sup>

Keil et al. experimentally analyzed multiple charging protocols (e.g., constant current—constant voltage, multistage constant-current, pulse charging, and a voltage-based trajectory) and their impact on the cycle life.<sup>38</sup> An ideal charging protocol must provide good capacity utilization with a minimal charging time while still holding a long cycle life. Among all the tunable parameters (C-rates or currents, voltage limits, number of stages and length of the pulses) in the protocol, the charging current was found to be the most significant one. Low current increases not only the capacity utilization but also the charging time. Fast charging can be achieved with high currents, but it deteriorates the cycle life mainly due to the occurrence of lithium plating.

**Operating voltage window.**—LIBs have a limited range of stability in terms of voltage and temperature.<sup>39</sup> Every combination of anode, cathode, separator and electrolyte materials defines a safe operating voltage window (VW). The optimal window represents the voltage range in which the cell delivers the maximum capacity without compromising its cycle life. Extending the voltage window, by overcharging<sup>34</sup> or overdischarging<sup>33,40</sup> the capacity delivered by the cell increases, but reduces the cycle life. Although, there is an extensive analysis of these two abuse scenarios, there are few studies of the cycle life of Li-ion cells in a reduced voltage window.

**Destructive physical analysis.**—Recent studies on Li-ion cells' performance focus on predicting their capacity fade,<sup>41</sup> state of health<sup>42</sup> and cycle life. From modeling<sup>43</sup> to experiments, multiple degradation mechanisms like SEI formation, lithium plating, degradation of the anode and cathode, etc. are attributed to the poor cycle life and in some rare occasions, actual evidence of those phenomena are presented. A straightforward solution is to physically open the cell and extract the components for further analysis. If this solution is not feasible, e.g., in a diagnostic test for secondary-use application, then a nondestructive technique is a better option. Electrochemical impedance spectroscopy (EIS),<sup>44</sup> X-ray computed tomography (XCT),<sup>45</sup> and neutron scattering<sup>46</sup> are noninvasive techniques that allow diagnosing, visualizing, and detecting, respectively, internal features in the cell without disrupting it. Even so, these noninvasive and inferential techniques do not provide the actual degradation imposed on the cell components affecting the actual cell performance and their implications on the safety aspects.

The goal of this work is to investigate the interplay between aging, operating voltage window, and abuse tests (overcharge and external short) in Li-ion cells and their safety implications. Part I focuses only on the aging effects in cylindrical Li-ion commercial cells that underwent charge/discharge cycling under nominal conditions. The objective is to characterize the changes occurring to the cell's electrochemical properties as well as its morphology as the cells aged. The aim is accomplished via charge/discharge cycling under two different voltage windows. The cells are aged up to 10%, 15% and 20% capacity fade (CF). The morphological changes are studied by conducting a destructive physical analysis (DPA) of the cell components and analyzing them via micrography (scanning electron microscopy, SEM) and spectroscopy (energy-dispersive X-ray spectroscopy, EDS) techniques. Part II analyzes the interaction between aging and the overcharge abuse test. Part III analyzes the interaction between aging and the external short abuse test. Cycling results for the aged cells that were also used for the studies reported in Part II and III are presented in the current work.

## Experimental

In this study, commercial cells of the NCR18650B type, considered the state of art for cylindrical cells,<sup>47</sup> are used to conduct this study. According to the manufacturer's specification, the cell nominal voltage is 3.6 V and the recommended safe operating voltage window is 2.7 to 4.2 V. The rated capacity is 3.4 Ah (minimum capacity of 3.2 Ah) when the cell is discharged to 2.7 V using a constant current (CC) protocol and then charged back to 4.2 V using a constant current—constant voltage (CCCV) protocol with a cutoff current of 65 mA.<sup>48</sup>

Prior to any aging or abuse test, it is necessary to discern the pristine condition of the cell components. Thus, the internal structure of a pristine cell is shown in Fig. 1a. The top of the cell corresponds to the positive terminal which is connected to the current collector of the positive electrode and the cell can is negatively polarized and is connected to the negative electrode. The current collector of the anode electrode is connected internally to the cell can by a nickel tab. The positive electrode for this cell design is nickel cobalt aluminum oxide,  $\text{LiNi}_{0.8}\text{Co}_{0.15}\text{Al}_{0.05}\text{O}_2$  (NCA) and the negative electrode is graphite (C). Electrodes and separators are assembled in a jelly roll around the central metal mandrel. There are two plastic insulators at the top and bottom of the jelly roll. The blue one (bottom) prevents contact between the jelly roll and the can (negatively polarized). While the brown one (top) prevents direct contact between the electrode roll and the nickel tab that connects

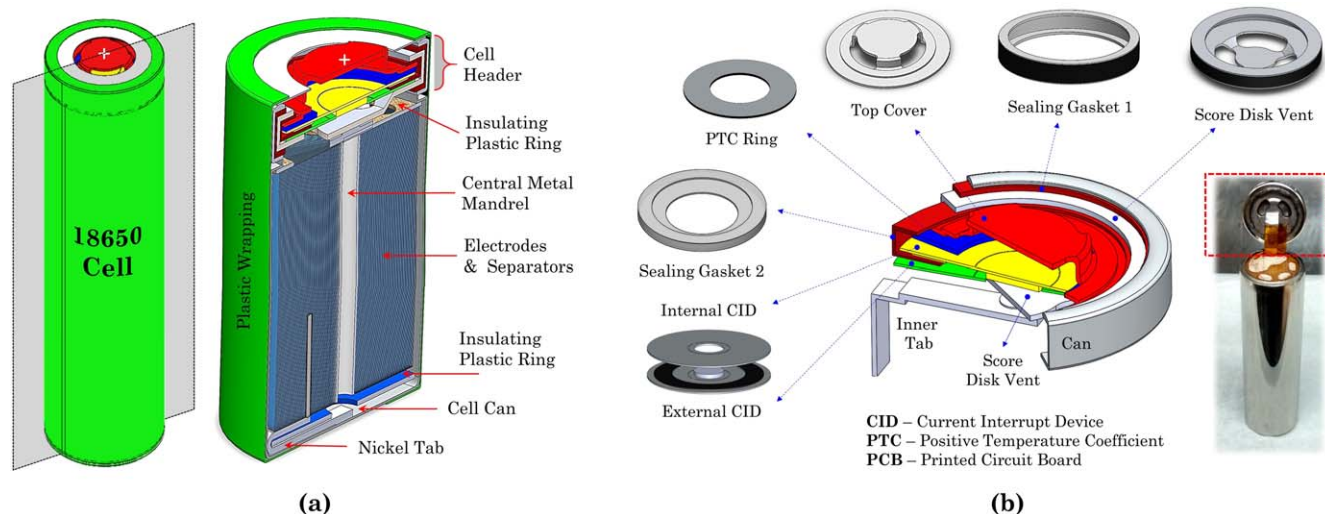


**Figure 1.** Schematic of a conventional cylindrical 18650 Li-ion cell with a spiral wound cell design. (a) Cross-section of the cell along the axial direction. (b) Cell header design showing the internal protective devices.

the positive electrode and current collector to the positive terminal. In the cell header, there is a protection for high currents (PTC, positive temperature coefficient) and high internal pressure (CID, current interrupt device). No PCB (protective circuit board) is included within the cell, Fig. 1b. The cell header is internally connected to the jelly roll via a nickel tab welded to the scored disk vent which is part of the CID.

**Conditioning test protocol.**—The cell status is monitored using a conditioning test protocol. Cells are cycled 3 times between 2.7 and 4.2 V at 1 C-rate. The charging process is done with a CCCV protocol and a cutoff current of 50 mA. The discharging process is done using a CC protocol. The internal resistance is calculated at 50% DOD (depth of discharge), based on the fresh cell capacity, by applying a 1.5 C (5.1 A) 100 ms pulse during the discharge step. The typical response of the commercial Li-ion cell to the conditioning test is shown in Fig. 2a. The current pulse excitation applied during the second cycle with its corresponding voltage response can be observed in Fig. 2a. By using the voltage before the pulse and the lowest voltage reached during the pulse period, see Fig. 2b, the internal resistance is calculated. The average internal resistance value at 50% SOC, of the 25 fresh cells used in this study is  $\sim 44$  m $\Omega$ .

**Cycling protocol.**—Based on the recommended operating conditions given by the manufacturer two different voltage ranges were selected. The “normal” operating window is defined in the range of [2.7, 4.2] V. This range is shortened by 200 mV on each end of the cutoff voltages. Thus, a “reduced” operating window is defined in the range of [2.9, 4.0] V. Cells cycled in the normal and reduced voltage window are denoted from hereafter as “N” and “R”, respectively. Cycling is done using a C/2 current for charging and discharging. Charge process to the corresponding upper voltage is done with a CCCV protocol and a 50 mA cutoff current. Discharge process to the corresponding lower voltage is done using a CC protocol. Cycling test is conducted at ambient temperature ( $\sim 23$  °C). The completion criterion for cycling is based on the capacity fade. For each cell, the capacity fade is defined with respect to the capacity obtained during the first complete discharge. Prior to and after the cycling test, each cell is electrochemically characterized using the conditioning test described earlier. Conditioning and cycling tests are conducted using a battery tester (Arbin system, BT2543-5V-5A-16). The cell temperature is measured on the cell surface, during the

cycling test, by means of a J-type thermocouple (Omega, TJ72-CPSS-116U-6) taped on the cell surface in the axial direction.

## Results and Discussion

A typical cell response to the conditioning test is shown in Fig. 2a. In a fresh new cell, lithium is stored in two main components, the electrolyte, and cathode. In the cathode material, intercalated lithium can be found in the lattice sites, while, lithium ions in the electrolyte are provided by the salts (LiPF<sub>6</sub>, LiBF<sub>4</sub>, LiAsF<sub>6</sub>) dissolved in the solvent, usually carbonates. In a pristine condition, graphite stores no lithium. Aurbach et al. demonstrated that in the presence of organic solvents, lithium and graphite are thermodynamically unstable.<sup>49</sup> The side reactions between lithium, more specifically lithiated graphite and the electrolyte solution lead to the formation of the SEI passivating layer. The conditioning test has two purposes: (a) establishing the actual cell capacity, and (b) allowing the cell to form a protective and stabilizing chemical SEI layer. Even though cells are fabricated in a similar fashion, there still exists a cell to cell variation that must be taken into account to define the capacity fade in the cell during the aging process. Meanwhile, SEI formation is a necessary step that prevents a continuous exfoliation of the active material as well as electrolyte decomposition.<sup>50</sup>

**Cycling.**—Representative voltage, current and temperature response for the cycling test during the first 40 h is shown in Figs. 3a and 3c for the normal and reduced voltage window, respectively. The percentage of capacity fade is defined by comparing of the capacity obtained during cycling to the maximum discharge capacity obtained during the second full cycle. The capacity values during the first cycle are typically not considered since the initial SOC at the beginning of the test may vary from cell to cell. The initial capacity for all the cells is listed in Tables I and II. Figure 3 also shows one current pulse applied after the cell was discharged to 50% of the discharge capacity obtained during the conditioning test. Fixing the discharge capacity percentage is the most objective way to compare the cells from both the normal and reduced voltage. Figures 3a and 3c shows that reducing the voltage window not only reduces the charge and discharge time but also the capacity utilization from the cell. Meanwhile, Figs. 3b and 3d shows the charge/discharge profiles at 5 different levels of capacity fade and the cycle number when they take place. Interestingly, the reduction of the delivered capacity from the cells cycled in the reduced voltage window comes along with an

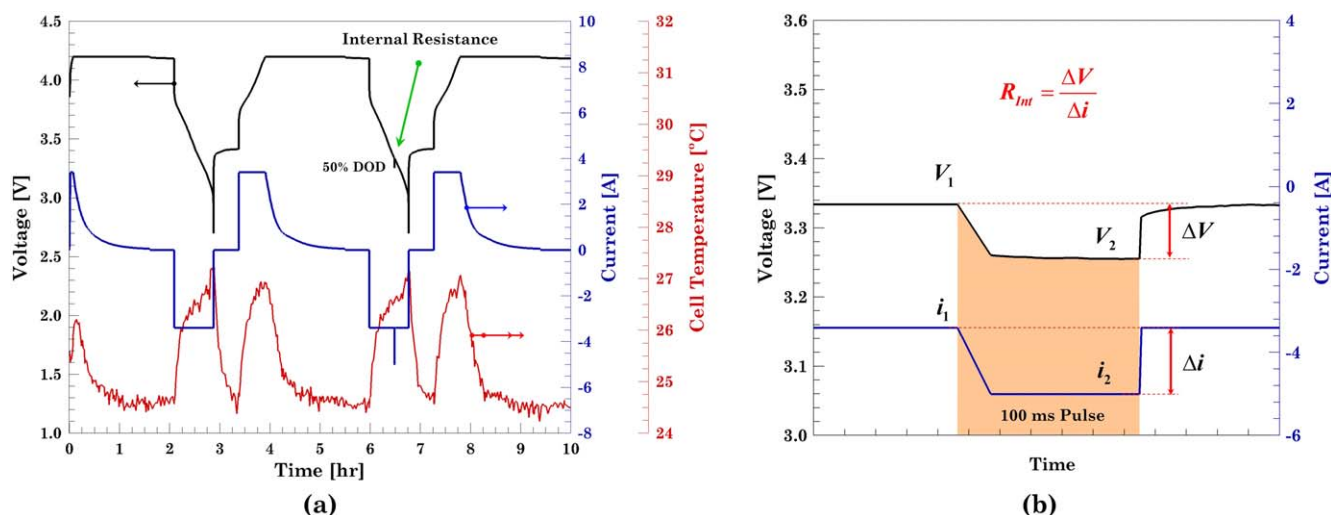


**Figure 2.** Representative results obtained from the conditioning test conducted in a fresh cell. (a) Voltage and current response. (b) Internal resistance calculation by applying Ohm's law,  $R = \Delta V / \Delta i$ , during the current pulse response.

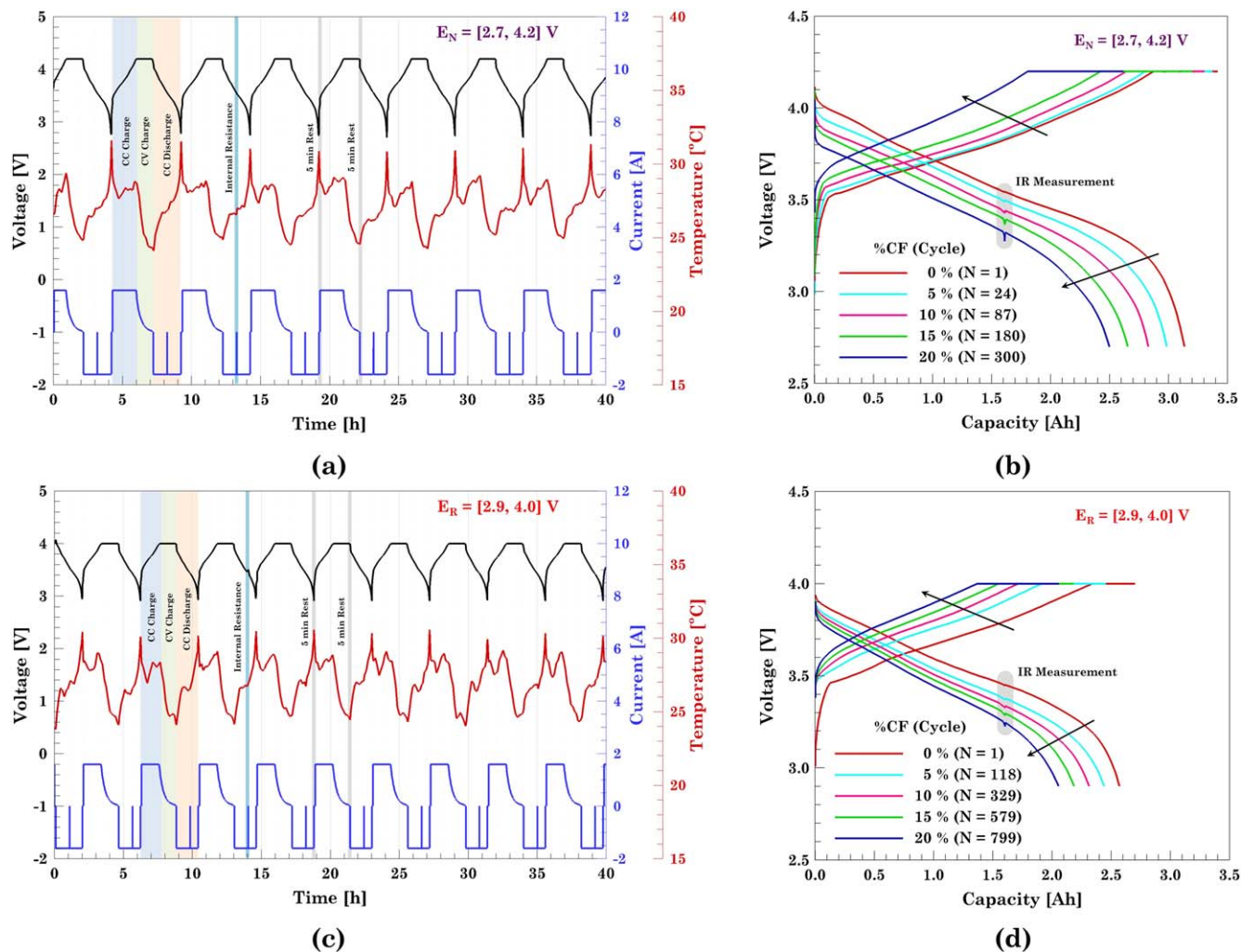


**Figure 3.** Electrochemical performance results for the aging test under the two voltage windows. (a)–(b) Comparison of the first 40 h for two representative cells cycled under the normal ( $N_{20}OV_1$ ) and reduced ( $R_{20}NA_1$ ) voltage window. (c)–(d) Charge/discharge voltage profile evolution as the cell cycling life diminishes 20% with respect to their corresponding initial discharge capacity.

extension of the cycle life. In the end, it is a tradeoff between capacity utilization and cycle life. Reducing the voltage window by 200 mV above and below the manufacturer recommended cutoff voltages extends the cycle life more than two times. Another subtle detail shown in the voltage profiles, during the internal resistance measurement, is the voltage response. The cell cycled under the normal voltage window exhibits a larger voltage change in comparison to the reduced one. Since  $\Delta V$  is proportional to the cell internal resistance, and internal resistance has a strong and direct relation with the cell degradation, this indicates that the cell cycled under the normal voltage window degrades faster than the reduced one. Cells

degradation rates and internal resistance evolution is discussed in more detail later.

Tables I and II summarize the final status of all cells at the end of the cycling test. For each voltage window, three capacity fading percentages are selected: 10%, 15%, and 20%. For each of the capacity fade percentages, either an overcharge (OV) or external short (EX), was conducted. The cells labeled as “NA” were not subjected to any abuse test after being aged. Thus, a cell labelled as  $N_XOV_Y$  indicates that the cell Y is cycled under the normal voltage window until its capacity fade was X%. After that, the cell was subjected to an overcharge test. Electrochemical results for all the 18

**Table I.** Cycle life summary for the cells aged in the normal voltage window,  $E_N = [2.7, 4.2]$  V.

Cell ID	Number of Cycles	Aging Test Time [Days]	Initial/Final Capacity [Ah]	Final/Goal Capacity Fade	Safety Test
$N_{10}NA_7$	174	36.83	3.032/2.710	10.59%/10%	No Abuse
$N_{15}NA_{10}$	222	54.18	3.228/2.728	15.49%/15%	No Abuse
$N_{20}NA_5$	269	56.60	3.243/2.590	22.97%/20%	No Abuse
$N_{10}OV_8$	201	47.22	3.129/2.765	11.63%/10%	Overcharge
$N_{15}OV_3$	199	48.21	3.192/2.700	15.41%/15%	Overcharge
$N_{20}OV_1$	300	89.94	3.138/2.499	20.36%/20%	Overcharge
$N_{10}EX_9$	204	47.22	3.137/2.803	10.64%/10%	External Short
$N_{15}EX_4$	234	56.08	3.204/2.724	18.25%/15%	External Short
$N_{20}EX_2$	305	89.94	3.227/2.469	23.48%/20%	External Short

**Table II.** Cycle life summary for the cells aged in the reduced voltage window,  $E_R = [2.9, 4.0]$  V.

Cell ID	Number of Cycles	Aging Test Time [Days]	Initial/Final Capacity [Ah]	Final/Goal Capacity Fade	Safety Test
R <sub>10</sub> NA <sub>11</sub>	<b>454</b>	78.76	2.522/2.218	<b>12.05%</b> /10%	No Abuse
R <sub>15</sub> NA <sub>10</sub>	<b>616</b>	105.53	2.618/2.208	<b>15.65%</b> /15%	No Abuse
R <sub>20</sub> NA <sub>7</sub>	<b>799</b>	142.37	2.570/2.055	<b>20.01%</b> /20%	No Abuse
R <sub>10</sub> OV <sub>5</sub>	<b>267</b>	50.50	2.562/2.304	<b>10.07%</b> /10%	Overcharge
R <sub>15</sub> OV <sub>3</sub>	<b>651</b>	115.95	2.567/2.175	<b>15.26%</b> /15%	Overcharge
R <sub>20</sub> OV <sub>1</sub>	<b>787</b>	143.56	2.565/2.046	<b>20.22%</b> /20%	Overcharge
R <sub>10</sub> EX <sub>6</sub>	<b>324</b>	60.04	2.553/2.291	<b>10.26%</b> /10%	External Short
R <sub>15</sub> EX <sub>4</sub>	<b>647</b>	115.95	2.555/2.159	<b>15.50%</b> /15%	External Short
R <sub>20</sub> EX <sub>2</sub>	<b>785</b>	143.05	2.567/2.049	<b>20.19%</b> /20%	External short

aged cells listed in Tables I and II are presented in Part I of this article. However, not all the DPA results are included here. Part I only accounts for the pure aging effect of cycling, hence the DPA results for only the 6 cells tagged as  $N_X NA_Y$  and  $R_X NA_Y$  are presented here. The DPA results for the overcharged (6 cells,  $N_X OV_Y$  and  $R_X OV_Y$ ) and externally shorted (6 cells,  $N_X EX_Y$  and  $R_X EX_Y$ ) cells at the end of the respective capacity fade periods are presented in the Parts II and III of the publication series, respectively.

The initial capacity of the cells ranges from 3.03 to 3.24 Ah, for the normal VW; and from 2.52 to 2.61 Ah, for the reduced VW, as shown in Tables I and II. The fact that there are three cells allotted to each of the capacity fade percentages gives the range in terms of the minimum and the maximum number of cycles that can be obtained from the cells. Thus, for the normal VW, it takes at least 174 cycles until the cell capacity fades more than 10.59%. The cell can be cycled almost 300 times before its discharge capacity drops below 20% the initial capacity. On the other hand, for the reduced VW, the cell can undergo 267 cycles before achieving 10.07% of capacity fade and it takes 785 cycles to get a 20% capacity fade. To put it in terms of real operating conditions, cells aged under the normal VW can be continuously cycled for almost 90 d delivering  $\sim 3.2$  Ah, at the beginning, and 2.4 Ah at the end of its cycle life (at 20% capacity fade). Whereas, a cell aged under the reduced VW can be continuously cycled for almost 143 d delivering  $\sim 2.5$  Ah, at the beginning, and 2.0 Ah, at the end of its cycle life. This means the cycle life can be extended by more than 50 percent if the VW is reduced.

Differential voltage plots, shown in Fig. 4, are derived from the CC steps of the charge/discharge profiles via a numerical differentiation. Data noise is removed by mathematical filtering to enhance the peaks from the  $dV/dQ$  plots. Multiple interpretations can be given to the differential voltage plots when combined with the respective differential analysis of the anode and cathode potentials. They can be used to detect the phase transitions<sup>51</sup> and the active mass evolution of the individual electrodes<sup>52</sup> with respect to the capacity. A different interpretation is given to the full cell differential voltage. Considering the constant current curves,  $I = dQ/dt$ , where  $I$  is the applied current,  $Q$  is the capacity, and  $t$  is the charge and discharge time. Also, the cell internal resistance relates to the cell overpotential,  $\eta$ , by  $\eta = IR_{int}$ . And, the full cell voltage can be expressed as  $V = \eta + OCV$ . Combining all the expressions, the differential voltage is deconvoluted in two contributions:

$$\frac{dV}{dQ} = \frac{d(OCV)}{dQ} + \frac{dR_{int}}{dt} \quad [1]$$

The first term is inherent to the thermodynamic equilibrium of the cell and the second accounts for the change in the internal resistance. The first term mainly depends on the SOC and the operating temperature and both these terms do not vary from one cycle to the next and hence can be considered to be constant. The second term is the relevant one for this work since it relates to cell degradation. The slippage voltage shown in Fig. 4, represented by

the shift of the two main peaks, directly relates to the aging degradation. The two peaks represent mainly the phase transition for the graphite electrode.<sup>51</sup> Electrode degradation induces an increment in the transport resistance in the solid phase. The large overpotential accelerates the phase transition at an early SOC, shifting the peaks (right to left) in the  $dV/dQ$  plots. During charge, no evident trend is found for the transition from  $Li_xC_{32}$  to  $Li_xC_{12}$ .<sup>53</sup> However, as the capacity and the SOC increases, the graphite phase transition from  $Li_xC_{12}$  to  $Li_xC_6$  is more evident. The effect of the voltage window is reflected in the number of peaks, i.e., in the number of graphite phases and transitions among them. Shrinking the voltage window reduces the number of graphite phases present during cycling.

The effect of the voltage window on the cycle life is more evident in the capacity retention plot shown in Fig. 5. The discharge capacity for the 18 cells is shown in Fig. 5a. Cells cycled in the normal VW clearly provide a larger capacity in comparison with the ones cycled in the reduced VW. The discharge capacity gets a  $\sim 600$  mAh reduction when the VW is reduced by 200 mV above and below the manufacturer's recommended voltage range. The drawback of the increased capacity is the number of times that the cell can be cycled before its capacity fades more than 20% with respect to the initial capacity. The capacity retention plots, Fig. 5b, the normalized version of the discharge capacity plots, give a more objective comparison of the cycle life. These plots reaffirm the fact that the cell cycle life can be considerably extended by reducing the capacity utilization from the cells. Thus, the mean number of cycles for the reduced VW is more than double the number for the normal voltage range as shown in Fig. 5d.

Besides the capacity retention, the internal resistance is another way to estimate the state of health of the cells. There is a common consensus that the internal resistance increases as the cell starts degrading. The remaining question is how fast the cell degrades or equivalently, at what rate does the internal resistance increase. Recent studies by Mandli et al. have proposed a linear increasing trend for this rate.<sup>54</sup> Present experimental results show a slightly different story, the internal resistance increases faster at the beginning of the aging test, then it slows down, and at about 80% of the capacity retention, it starts increasing again.<sup>55</sup> The initial increment of the internal resistance is attributed to the continuous formation of the chemical and electrochemical SEI.<sup>56</sup> The linear capacity fade is attributed to the SEI growth. As the cycling continues, the passivating layer becomes quasi-stable on the graphite electrode. Then, non-uniform intercalation/deintercalation (lithiation/delithiation) leads to local pore clogging near the interface between the anode and the separator. Yang et al. attribute the lithium plating and nonlinear capacity fade to the anode porosity drop.<sup>57</sup> Thus, non-uniform lithiation/delithiation process induces stress on both active materials, disrupts the electrode morphology, increases the transport resistance and consequently the cell internal resistance.<sup>58</sup>

In order to determine the point at which the cell degrades at a faster rate, experimental data from all cells are used to fit an overall curve for each of the two state of health (SOH) indicators (capacity

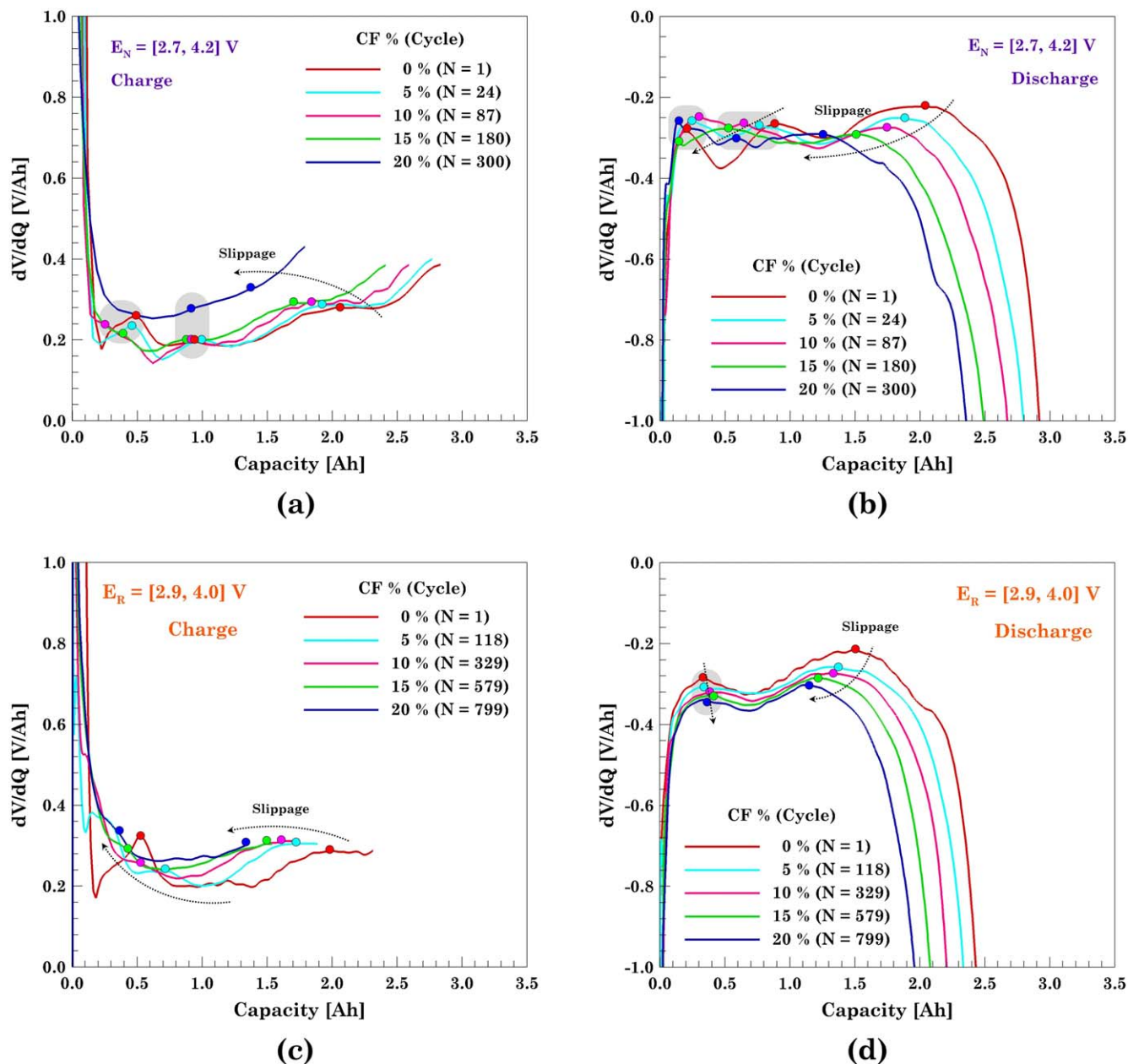


**Figure 4.** (a)–(d) Differential voltage analysis of charge and discharge profiles for cells  $N_{20}OV_1$  and  $R_{20}NA_1$  cycled under the normal and reduced voltage window, respectively.

fade and cell internal resistance). The individual CF and IR plots are the deciding factors in the selection of the function that better fit the experimental results. Thus, a third-degree polynomial function is used to obtain the general curves for both voltage windows. The fitted equations for both, the normal and reduced VW cells, are included in Fig. 5e with the corresponding curves. The faster degradation happening in the cells cycled under the normal VW becomes more evident with fast capacity decay and an accelerated increase on the cell internal resistance. The differential CF and IR curves, with respect to the number of cycles, provide an estimation of the moment when the cell begins to degrade at a faster rate. Two points are of interest in these differential plots. In the differential internal resistance, the minimum point marks the point at which accelerated degradation starts. For the cells aged under the normal VW, this minimum point occurs at cycle 127, when the discharge capacity has faded 11.2%. The large variation in the necessary number of cycles to achieve 10% or 20% CF can be explained by the fact that the 9 cells listed in Table I are already degrading at a faster

rate. In the case of the cells aged under the reduced VW, the minimum point occurs at cycle 511, when the discharge capacity has faded about 15.0%. For that reason, it takes roughly 150 cycles, to degrade the cell from 15% to 20% CF as shown in Table II.

**Thermal response.**—There is a strong correlation between the internal resistance and a cell's thermal response. Cells with high internal resistance than what their design entails are more prone to have a higher temperature during cycling. The morphological differences between the electrodes lead to an uneven temperature response during charge and discharge.<sup>59</sup> Thus, the maximum temperature rise happens during discharge and hence only these curves are analyzed. To put it in perspective, Figs. 6a and 6b show the cell thermal response during discharge at different degradation levels ranging from 0% to 20% CF, for one representative cell aged under each VW. When the cells are fresh, the cell increases its temperature by 7 °C and 6 °C, for the normal and reduced VW, respectively. As the cell degrades, the temperature increment rises to

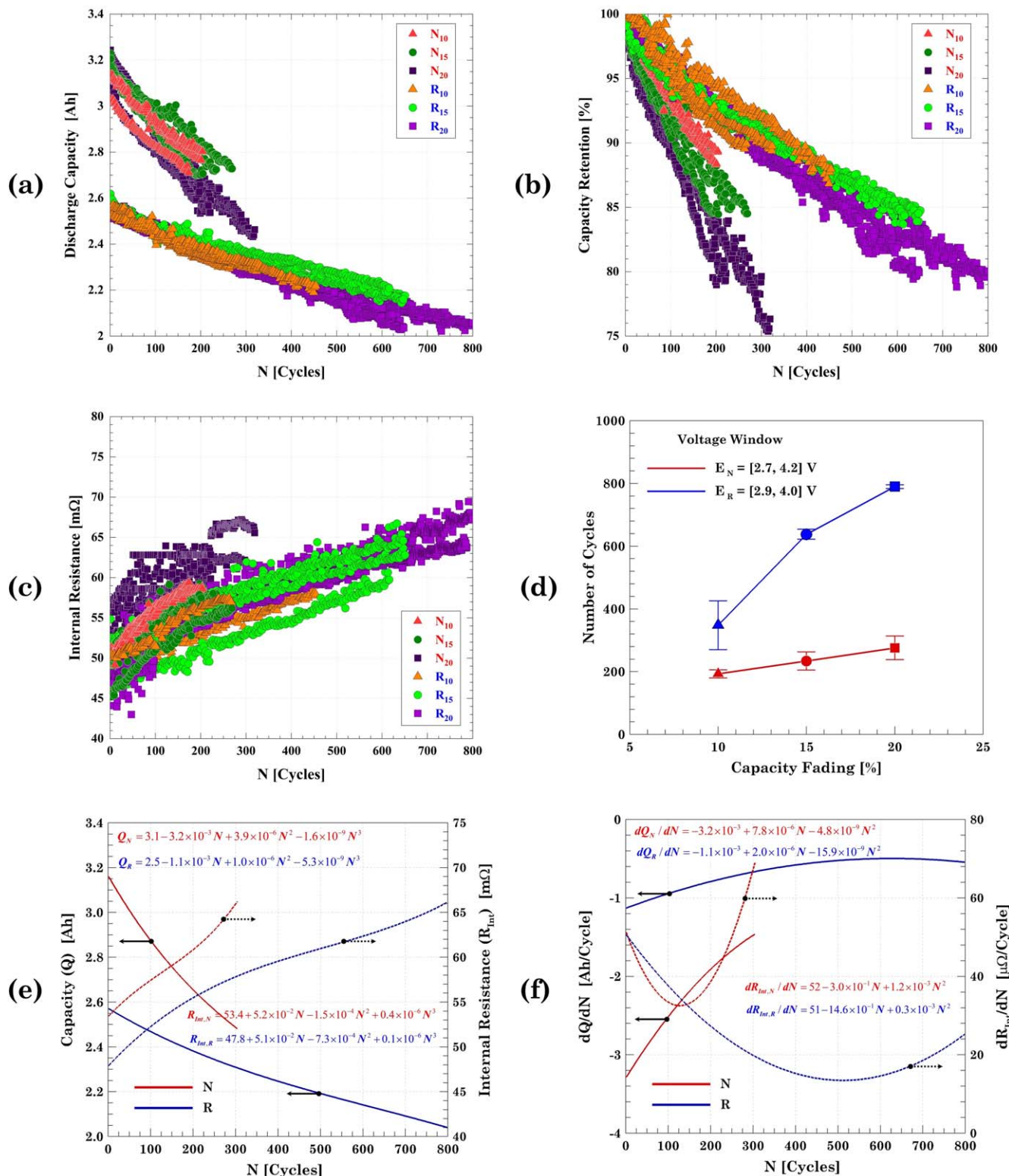


**Figure 5.** (a) Discharge capacity, (b) capacity retention, and (c) internal resistance evolution through aging for all the cells from this study. (d) Average number of cycles required to achieve 10%, 15% and 20% capacity fade as a function of the voltage window. (e) Capacity fade and internal resistance trend; (f) capacity and internal resistance change per cycle.

9.5 °C and 8.5 °C, respectively. The temperature rise is a consequence of the heat generated by the cell due to the electrochemical reactions and the charge transfer taking place during the charge and discharge process. As the cell degrades, irreversible chemical and electrochemical reactions, e.g., SEI growth and electrolyte decomposition, as well as the morphological changes,

such as fracture of the active particles, hinder the charge transfer between the electrodes. The degradation phenomenon affects the transport processes, increases the cell internal resistance and alters the heat generated by the cell.

Heat generation has two main components, Joule heating (irreversible) and entropic heating (reversible).<sup>60</sup> At low C-rates,

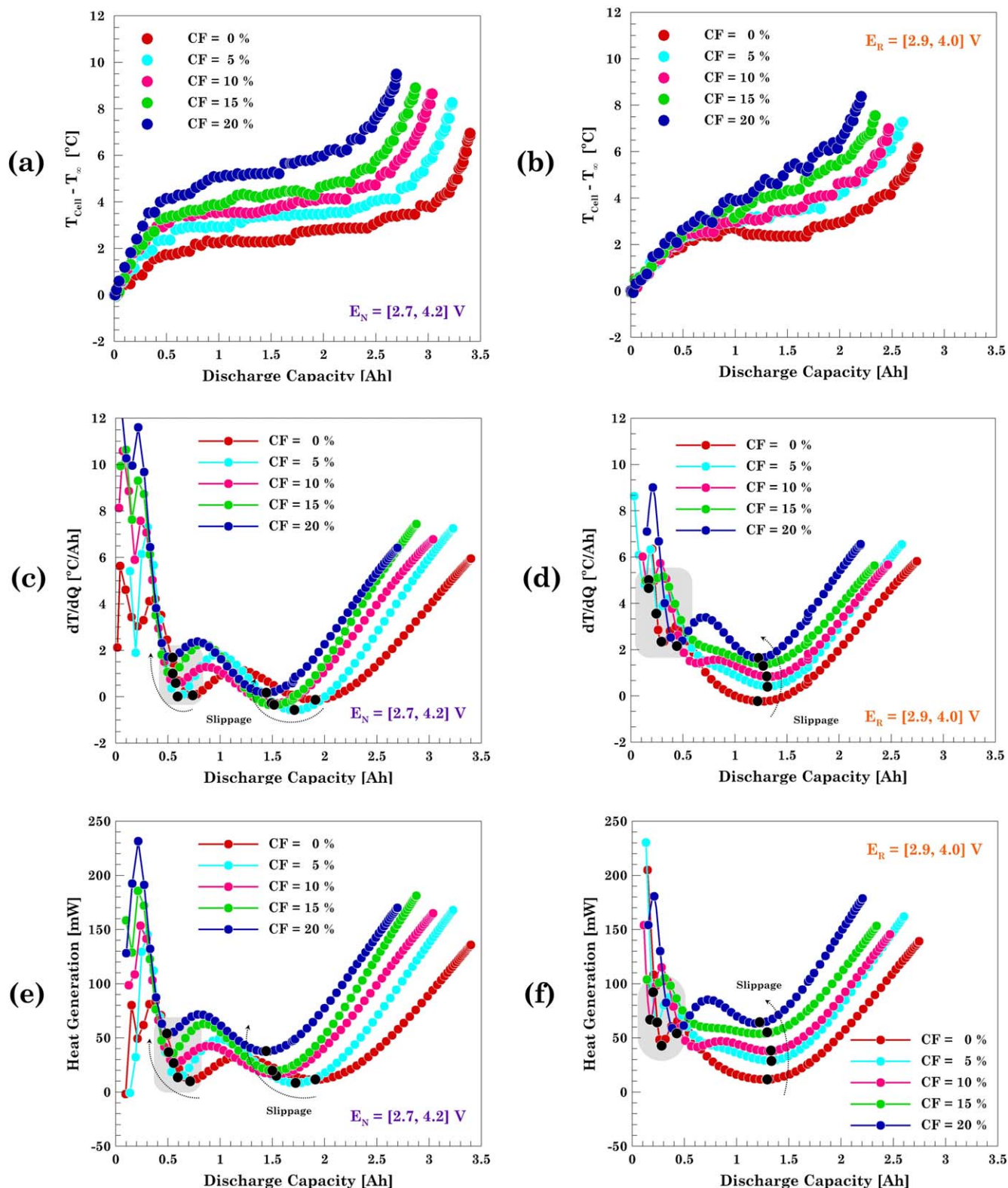


**Figure 6.** Experimental thermal response of the cells as a function of the capacity fade percentage and the voltage window for the discharge process. (a)–(b) Cell skin temperature increment with respect to the environmental temperature. (c)–(d) Rate of temperature change with respect to capacity. (e)–(f) Heat generation estimated via an inverse problem calculation using the temperature profile during discharge.

the irreversible heat is negligible, and the reversible heat is the predominant one. As the C-rate increases, the irreversible heat dominates and the reversible one becomes negligible. The aging test is done at a C/2 rate which is the rate recommended by the manufacturer; thence, it is reasonable to assume the heat generated

is mainly due to irreversible heat. Joule heating can be calculated in terms of the electrical current and the average internal resistance ( $\dot{Q}_{irrev} = I^2 R_{int}$ ). Instead, the inverse heat transfer method proposed by Mistry et al. is used to estimate the cell heat generation using the temperature profile.<sup>60</sup> The energy balance for the cell includes the

energy stored by the cell, the heat generated, and the energy dissipated by the convection mode and it can be expressed as:

$$mc \frac{dT}{dt} = \dot{Q} - hA(T - T_{\infty}) \quad [2]$$

here  $m$  is the mass of the cell ( $m = 0.044$  kg),  $c$  is the heat capacity ( $c = 837$  J (kg K)<sup>-1</sup>),<sup>60</sup>  $A$  is the cell surface area ( $A = 4.184 \times 10^{-3}$  m<sup>2</sup>),  $T$  is cell temperature in (°C),  $T_{\infty}$  is the environmental temperature,  $h$  is the convective heat transfer coefficient (W (m<sup>2</sup>K)<sup>-1</sup>), and  $\dot{Q}$  is the heat generated by the cell (W). It is important to note that the variable  $Q$  does not represent heat but rather the cell capacity. No temperature variation in the radial direction is considered since  $Bi = 0.013 < 0.1$ , assuming a thermal conductivity of  $k = 3$  J (mK)<sup>-1</sup>. From all the properties in Eq. 2 only  $T$ ,  $\dot{Q}$ ,  $h$ , and  $T_{\infty}$  varies with time. To account for this variation, the cell temperature is fitted by the analytical expression in Eq. 3.

$$T = c_0 + \sum_{i=1}^N c_i e^{-t/\tau_i} \quad [3]$$

The time constants ( $\tau_i$ ) in the exponential function are geometrically distributed between the Nyquist frequency and the convection time constant, i.e.,  $\tau_i \in [\tau_{\min}, \tau_{\max}] = [2/f_s, mc/hA]$ . The number of terms,  $N$ , is estimated via a sensitivity test. The coefficient of determination,  $R^2$ , between the experimental and the fitted values is the decision parameter to select  $N$ .

Ambient temperature cannot be assumed as constant since the cell is exposed to the environment. Thus, the ambient temperature is collected along with the cell temperature. During the rest period, after the discharge process, there is no heat generation, i.e.,  $\dot{Q} = 0$ . Hence, the convective heat transfer coefficient,  $h$ , for a specific degradation level, can be calculated from Eq. 2 using the corresponding temperature profile decay. The estimated  $h$  values vary as  $h \approx 9 \sim 20$  W (m<sup>2</sup>K)<sup>-1</sup> corresponding to a Biot numbers of  $Bi \approx 0.011 \sim 0.026 < 0.1$ . At this point, the unknown heat generation for the  $T$  curves shown in Figs. 6a and 6b is calculated and the results are shown in Figs. 6e and 6f. The differential temperature,  $dT/dQ$ , can be correlated to the energy stored by the cell,  $mc \frac{dT}{dt}$ , by scaling it by a factor of  $1/(mcI)$  factor, where  $I$  is the applied current. In other words, the stored energy can be estimated by differentiating the temperature response profile during charging and discharging.

As  $dT/dQ$  follows a similar trend as the heat generated, this indicates that the convective heat loss becomes quasi-constant and it only exacerbates at the end of the discharge. The rate of energy loss is much less than the heat generation rate leading the cell to self-heat.

Heat generation exhibits a SOC dependence, as shown in Figs. 6e and 6f, contrary to the idea of having a constant value ( $\dot{Q}_{irrev} = I^2 \bar{R}_{int}$ , where  $\bar{R}_{int}$  is the mean internal resistance value and  $\dot{Q}_{irrev}$  is the irreversible heat) throughout the whole SOC range. The heat generated increases when the cell reaches the fully charged and fully discharged condition. This is consistent with the internal resistance change ( $dV/dQ$ ), Figs. 4c and 4d, and its effect on the Joule heating effect. At these two extreme conditions, the internal resistance is maximized as well as the heat generated by the cell due to an increase in the cathode charge transfer resistance.<sup>61</sup> In the intermediate SOC range, the two local minima highlighted in Figs. 6e and 6f correlates with the graphite phase transitions. A maximum point in the  $dV/dQ$  curve, Figs. 4c and 4d, corresponds to a minimum cell internal resistance and consequently the cell generates the minimum amount of heat. As the cell ages and the electrodes degrade, there is a slippage of the heat generation points and the corresponding heat generated. As the cell ages, the extreme heat generation points occur at an early SOC and the heat generation increases.

**Post mortem analysis.**—At the end of the cycle life, cells are subjected to a destructive physical analysis aiming to determine the

extent of degradation in the cell. Electrodes (anode+cathode) and the separators are extracted from the aged cells, at the fully charged condition, using the procedure described in the Appendix A section, see Figure A-1. In order to have a baseline for the morphological/physical changes, a fresh cell is subjected to a DPA establishing the pristine condition of the cell components. In Figs. 7 and 8, the orientation and position of the electrode with respect to the center is highlighted since degradation is anisotropic.

The electrodes from the fresh cell (0% CF) are extracted as they come from the vendor. Cells are typically shipped at 30% SOC. Since the cell is at low SOC, its graphite electrode exhibits the characteristic purple-darkish color of the partially lithiated graphite,<sup>62</sup> see the 0% CF electrodes from Fig. 7. For this particular cell, NCA and graphite electrodes are double-side coated. An asymmetry is observed on the separator present in the cell with the side of the separator facing cathode displaying a ceramic coating made of aluminum oxide (Al<sub>2</sub>O<sub>3</sub>) and cross-linked ethylene-oxide chains, see separators from Fig. 8. The coated separator membrane blocks lithium dendrites from the anode crossing over to the cathode.<sup>63</sup> This ceramic coating spans only the area covered by the NCA electrode. The yellow stripe on the positive electrode is the nickel positive tab that connects the NCA electrode and the base of the CID. The yellow color comes from the insulating tape preventing any possible internal short.

Graphite electrodes extracted from aged cells (10%, 15%, 20% CF) exhibit the characteristic golden color of the fully lithiated state, see Fig. 7. Non-uniform lithiation is the leading factor behind graphite degradation. The dark-ish color in the central area of the electrode is a characteristic feature which indicates non-uniform lithiation. The degradation happening in the edge of the graphite electrode is less visible, but it plays a key role in the safety aspects. The active material on the edge becomes electrochemically inactive due to a phenomenon denominated as “anode seclusion effect.” Since the cathode is shorter than the anode there is no direct path for Li-ions to intercalate into the anode electrode at the edges. The lithium concentration gradient induced by charging and discharging the cell can be alleviated if the cell is allowed to rest for long time periods (days).<sup>64</sup> The 30-minutes rest period in between the charge and discharge process is not sufficient to reduce the concentration gradient and consequently there is a cumulative effect with cycling. Thus, the graphite electrode contributes to the cell capacity fade not only because of the SEI formation but also due to the electrochemical seclusion of its outer areas, as shown in the graphite electrodes cycled in the normal VW. In the case of the cell cycled in the reduced VW, the amount of lithium intercalated/deintercalated is much less; hence, the seclusion effect is less visible even for the cell aged until 20% CF. It is important to note that no lithium plating evidence was found on any of the electrodes.

The decaying electrochemical performance of the cell cannot be attributed only to the anodic electrode. The intercalation and deintercalation processes that occur between the graphite and the NCA electrode is also reflected in morphological degradation.<sup>59</sup> Non-uniformly lithiated areas in the graphite electrodes can be explained by looking at the counterpart regions in the NCA electrode. The cathode electrode does not have a colorimetric spectrum as does the anode; still, it is possible to distinguish the normal electrode and the degraded one. Pristine NCA electrode (0% CF) from Fig. 8, displays a shiny dark color under the light mainly due to calendaring. As the electrode ages and degrades, delamination of the outer layers near to the separator takes place exposing the inner layers of the electrode with the characteristic dull black color, as observed in the electrodes for the 10%, 15%, 20% CF from Fig. 8. Cathode delamination occurs due to stresses induced by the non-uniform intercalation/deintercalation of lithium ions. The stress creates microcracks on the active particles during the charge/discharge cycling process. Propagation of the microcracks compromises the mechanical stability of the active material in the long-term cycling and eventually leads to the NCA electrode delamination.<sup>65</sup> Non-lithiated areas in the central region of the graphite electrode are

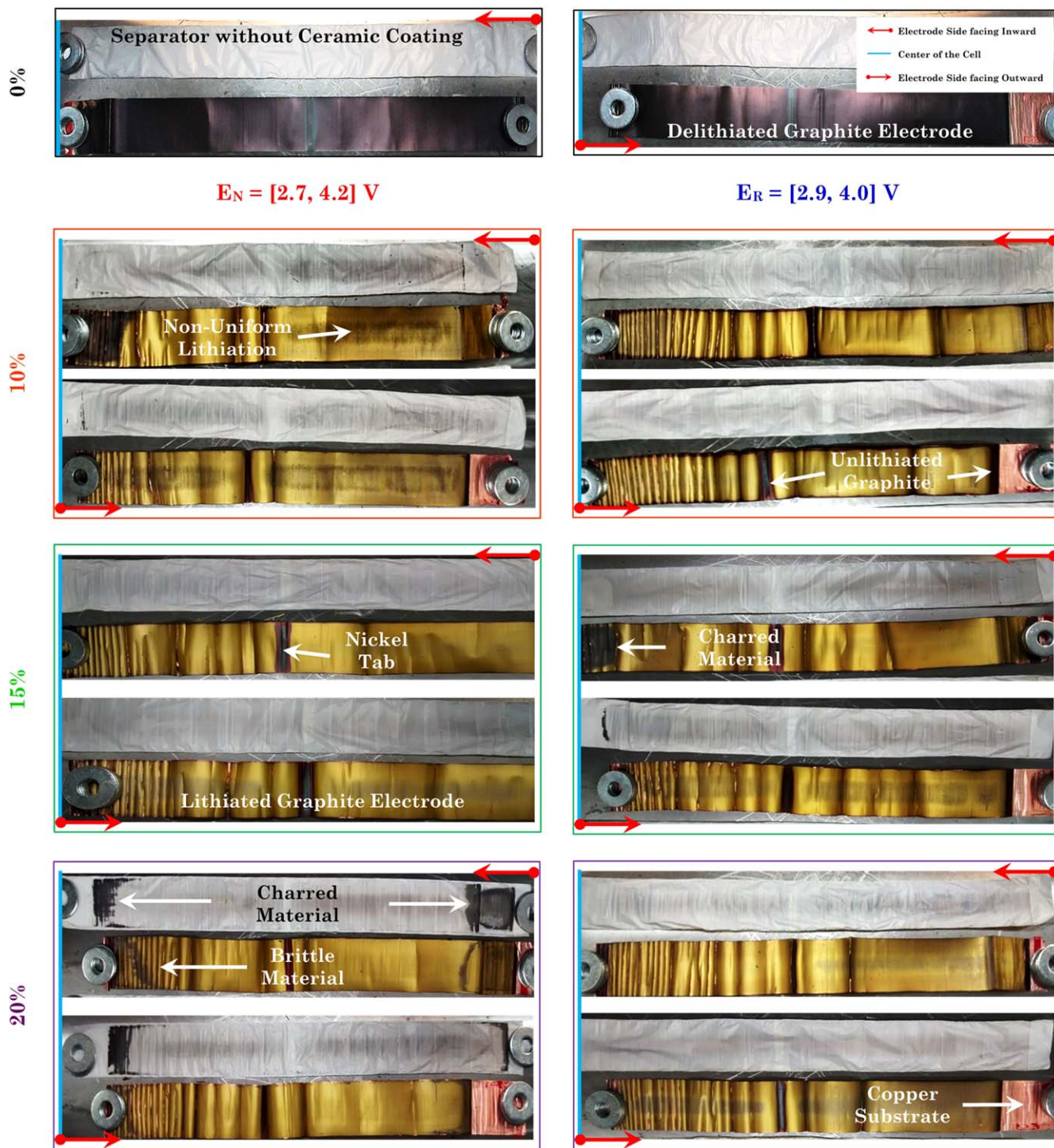


**Figure 7.** Graphite electrode's degradation with cycling for both studied voltage windows. Left column: Normal voltage window; right column: reduced voltage window. Percentage of capacity fade is shown on the left side. Each side of the electrode is identified according to their orientation with respect to the cell center and the side of the electrode facing it.

the consequence of the mechanical degradation of the cathode. Along with the mechanical degradation of the cathode, the  $\text{Al}_2\text{O}_3$  ceramic coating from separator prevents the lithium-ion from leaving the NCA electrodes by locally adhering to the cathode electrode and covering its surface. Thus, when the jelly roll is disassembled, the ceramic coating is observed to have adhered to the surface of the cathode in the areas that are in the middle of the axial length of the cell and these areas are more concentrated in the inner winds of the electrode roll. Another detail that was observed was that the delamination was more pronounced on the side of the cathode

active material that is facing the cell can compared to the side of the cathode facing the center of the cell. Delamination and cracking of the cathode and adherence of the ceramic coating to the cathode are leading contributors to the transport and kinetic resistance rise in an aged cell.

**SEM.**—Microstructural disruption associated with the aging process is investigated via microscopy and spectroscopy. So far, Figs. 7 and 8 have shown the macroscopic evidence of the electrode degradation. More insights about the real mechanisms behind the

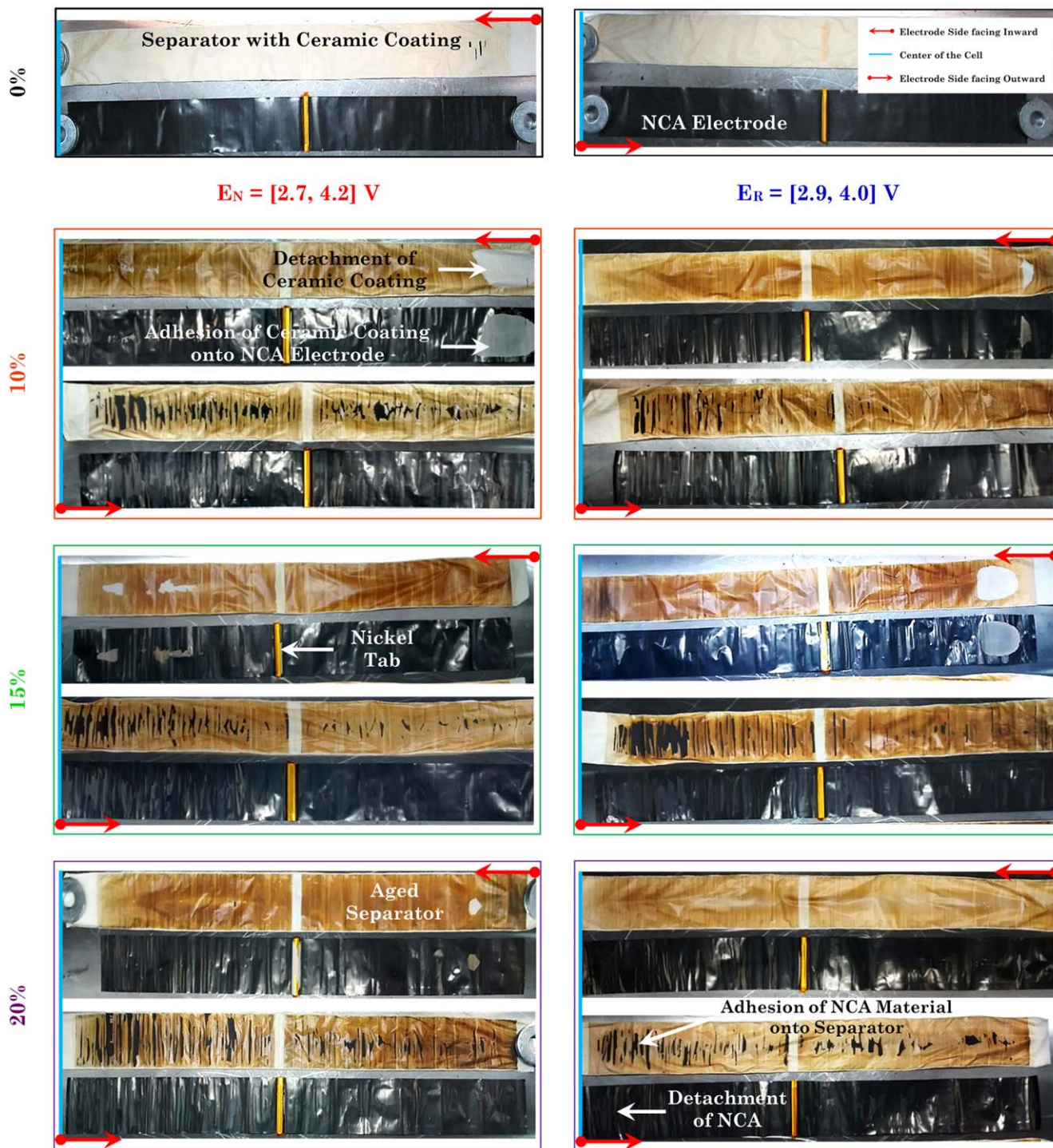


**Figure 8.** NCA electrode's degradation with cycling for both studied voltage windows. Left column: Normal voltage window; right column: reduced voltage window. Percentage of capacity fade is shown on the left side. Each side of the electrode is identified according to their orientation with respect to the cell center and the side of the electrode facing it.

degradation of performance can be found at the microscopic level. Lithiated graphite may look alike at the macroscopic level but they may differ at the microscopic level. Pristine samples (0% CF) harvested from the graphite and NCA electrodes are shown in Fig. 9 at low and high magnification. This provides details of a portion of the electrode at a low magnification as well as the individual particles at a higher magnification.

Pristine graphite has an amorphous platelet shape. The anode particle is made up of graphene layers where lithium ions can

intercalate in between the layers. In the pristine condition, it is possible to distinguish the boundary of the particle layers. As the cell ages (10% CF) and the electrode gets lithiated, intercalated lithium and SEI formation fill those gaps and the particle boundary disappears. Thickening of the SEI film becomes more evident in the cells aged to 15% of its capacity. The graphite active particles get covered with a thicker passivating layer and consume the lithium inventory reducing the available energy during discharge. When the cells reach the 20% CF, the differences between the VW used

## Graphite Electrodes

## NCA Electrodes

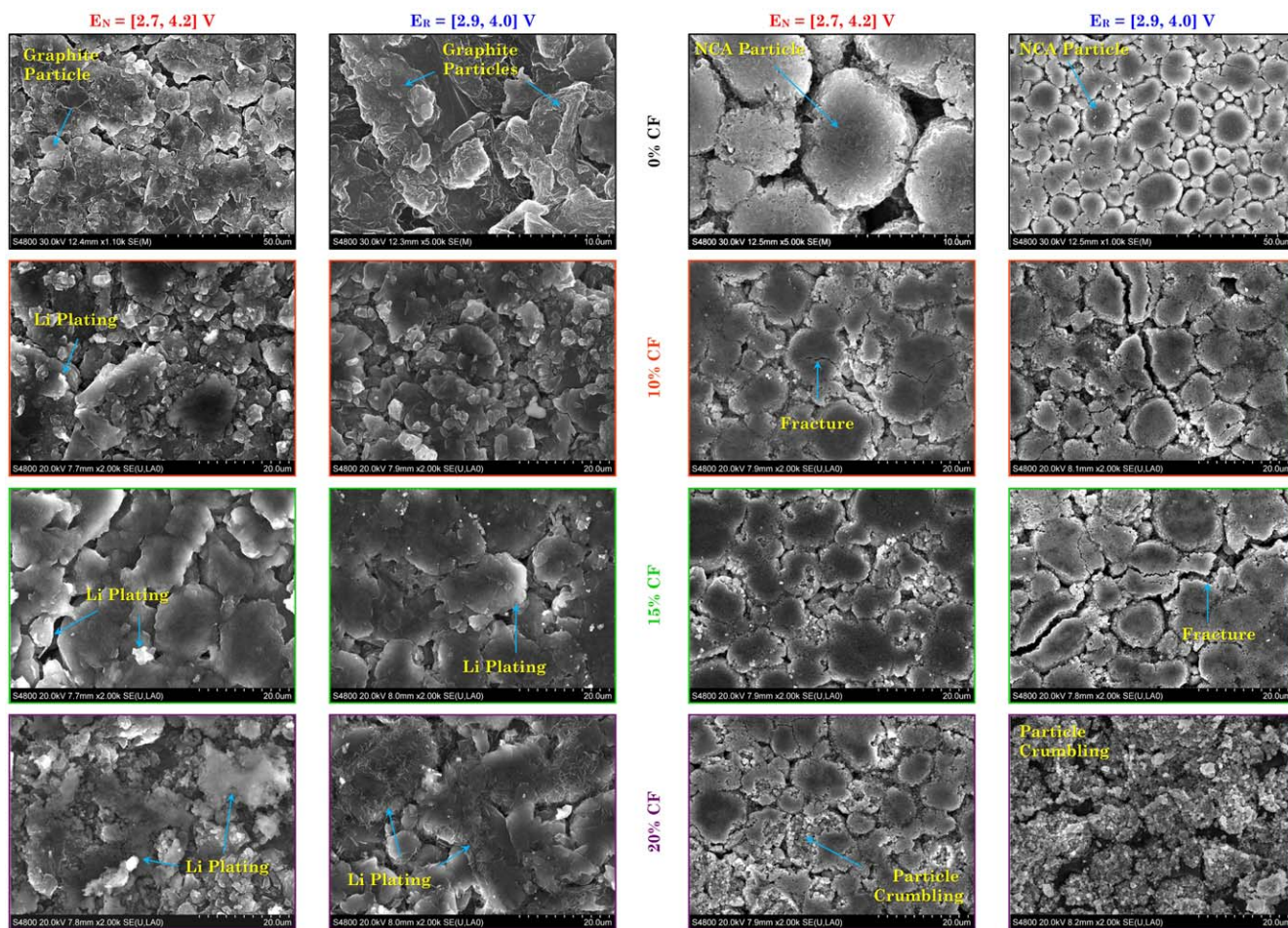


**Figure 9.** Micrographs of graphite (columns 1 and 2) and NCA (columns 3 and 4) representative samples harvested from the fresh and aged electrodes. For the fresh cell electrodes (0% CF), a 1 k $\times$  and 5 k $\times$  magnification images are shown. For the aged electrodes, only a 2 k $\times$  magnification is shown.

emerge. The electrode harvested from the cell cycled with the normal VW exhibits large deposits of lithium on its outer surface. Even more, the graphite particles break down due to the expansion/contraction during the intercalation and deintercalation of lithium ions. The non-uniform lithiation leads to the localized deposition of lithium plating which is more easily visible under the microscope. On the other hand, the electrodes from the cell cycled in the reduced VW, exhibit a finger-like formation on top of the SEI passivating layer. This would indicate an early stage for the lithium deposition.

The pristine NCA active particles are spherical agglomerates (mean diameter of 12  $\mu\text{m}$ ) of small particles. Its surface is flat indicating the electrode was calendared prior to the jelly roll assembly. Degradation on the cathode electrode can be chemical (electrolyte decomposition and reaction with NCA) and mechanical (fracture and agglomerate crumbling). Stress-induced by the non-uniform intercalation/deintercalation of lithium ions is the driving mechanism behind aging degradation. The fatigue effect can be interpreted in terms of the number of cycles as well as the voltage window. In the normal VW, the loading represented by the amount of lithium intercalated/deintercalated is large, which means more particles participate in the electrochemical reaction. As the cell ages, the electrode become more prone to fracture and eventually leads to the NCA material delamination. Delaminated material for practical purposes is electrochemically inactive and reduces the cell capacity utilization, the cycle life and turns the counterpart graphite region into a secluded area. In the reduced VW, the degradation of the

electrode is lower, and the stress that is induced, in this case, is reflected as a crumbling of the agglomerates on the surface.

**EDS.**—Chemical change on the electrode samples shown in Fig. 9 is done via EDS. The chemical composition of the graphite and NCA electrodes is shown in Table III and Table IV, respectively. The EDS shows carbon and fluorine as the major elements present where the composition of the pristine graphite electrode is carbon from the active material and the conductive additive and fluorine from the binder. The presence of copper comes from the current collector and the rest of the elements are from the electrolyte residuals. As the graphite electrode ages, the SEI keeps growing. The main compounds on the SEI layer are lithium carbonate ( $\text{Li}_2\text{CO}_3$ ), lithium hydroxide ( $\text{LiOH}$ ), lithium fluoride ( $\text{LiF}$ ), lithium oxide ( $\text{Li}_2\text{O}$ ), lithium alkyl carbonate ( $\text{ROCO}_2\text{Li}$ ,  $\text{RCOLi}$ ),<sup>66</sup> where R is an alkyl group made of carbon and hydrogen. Thus, in the cells aged with the reduced VW, the increment on the oxygen and fluorine percentage is due to the SEI formation. The passivating layer hinders the intercalation of the exposed graphite and reduces the carbon content detected in the sample. Similar behavior is found in the cells aged under the normal VW, with 10% and 15% CF. The sudden reduction in the carbon content and large increase on the oxygen level, in the cell with 20% CF, indicates the presence of lithium plating. Lithium plating is confirmed from the reaction of Li metal with air, when the sample is exposed to the environment, forming lithium hydroxide.

**Table III. Chemical composition (wt%) for the graphite electrodes harvested from fresh and aged cells under the two voltage windows,  $E_N = [2.7, 4.2]$  V and  $E_R = [2.9, 4.0]$  V.**

	Graphite Electrode									
	CF	C	O	F	P	Al	Ni	Co	Cu	
Fresh Cell	0%	74.9	23.4	1.1	0.2	0.1	0.0	0.0	0.3	
Normal	10%	42.4	36.5	18.4	1.7	0.7	0.2	0.2	0.0	
	15%	50.1	43.7	3.7	1.3	1.1	0.0	0.0	0.0	
	20%	29.0	49.2	17.6	2.8	1.1	0.0	0.1	0.0	
Reduced	10%	50.6	38.6	8.3	1.6	0.8	0.1	0.0	0.0	
	15%	54.7	34.0	8.5	1.9	0.5	0.3	0.1	0.0	
	20%	54.0	37.8	5.8	1.4	0.8	0.1	0.0	0.0	

**Table IV. Chemical composition (wt%) for the NCA electrodes harvested from fresh and aged cells under the two voltage windows,  $E_N = [2.7, 4.2]$  V and  $E_R = [2.9, 4.0]$  V.**

	NCA Electrode									
	CF	C	O	F	P	Al	Ni	Co	Cu	
Fresh Cell	0%	0.0	32.2	0.0	0.0	1.2	55.6	11.0	0.0	
Normal	10%	17.6	24.6	2.3	0.3	4.7	41.9	8.5	0.0	
	15%	12.5	27.1	3.8	2.9	3.3	41.5	8.7	0.0	
	20%	13.0	24.5	4.1	0.3	3.2	45.3	9.5	0.0	
Reduced	10%	13.7	24.8	5.9	0.4	2.6	44.0	8.4	0.0	
	15%	15.8	27.6	0.1	0.1	5.5	42.4	8.3	0.0	
	20%	9.8	28.4	0.6	0.7	17.1	36.7	6.7	0.0	

The chemical composition of the pristine NCA electrode confirms the presence of nickel (Ni), cobalt (Co), aluminum (Al) and oxygen (O). As the cathode electrode ages, the percentage of Ni and Co decreases due to the byproducts of the reaction of the oxygen in the cathode with the carbonate solvents from the electrolyte. This explains the reduction of the oxygen percentage and the rise of the carbon percentage. The adherence of the ceramic coating from the separator on to the NCA electrode is reflected as an increment of the Al percentage.

### Conclusions

In this work, a comprehensive work on the analytics of degradation with cell aging is presented. The work comprises experimental and analytical data for the electrochemical, thermal, chemical and morphological aspects of the Li-ion cells' components. The work is divided into three parts with the first one focusing on the aging degradation aspects with only charge and discharge cycling. The implications of the safety aspects associated with the overcharge and external short scenarios of cycled cells will be presented in Part II and Part III. Present results set the baseline to study and compare the safety implications of an aged cell when subjected to continuous charge/discharge cycling which involves just the nominal electrochemical processes.

The effect of the aging mechanism at three degradation levels (10%, 15%, and 20% CF) is investigated. Long-term cycling under two voltage windows, normal ( $E_N = [2.7, 4.2]$  V) and reduced ( $E_R = [2.9, 4.0]$  V), are tested. The cells cycled in the reduced VW gives more than double the cycle life compared to the ones cycled in normal VW one. The lifetime extension comes along with a reduction of 20% of the capacity utilization.

The degradation mechanisms behind the cell capacity fade are the SEI growth on the anode side and delamination and fracture of the cathode and adherence of the ceramic coating from the certain separator areas onto the cathode surface. SEI formation on graphite consumes lithium inventory. Delamination induces a partial electrochemical deactivation of cathode and seclusion of the anode

counterparts. The non-uniform lithiation/delithiation on these areas lead to early stages of lithium plating especially on the cells aged more than 20% CF. The departure of the electrodes from their pristine condition translates at the cell level as an increment on the internal resistance and the Joule heating effect. The thermal response of the cell is found to be SOC dependent with a maximum irreversible heat generation at 0% and 100% SOC.

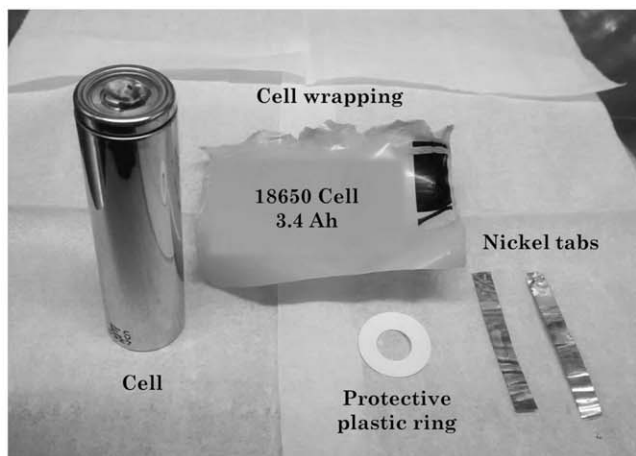
### Acknowledgments

Financial support from Underwriters Laboratories Inc. (UL) is gratefully acknowledged. The use of the scanning electron microscopy facility at the Birk Nanotechnology Center, Purdue University is acknowledged.

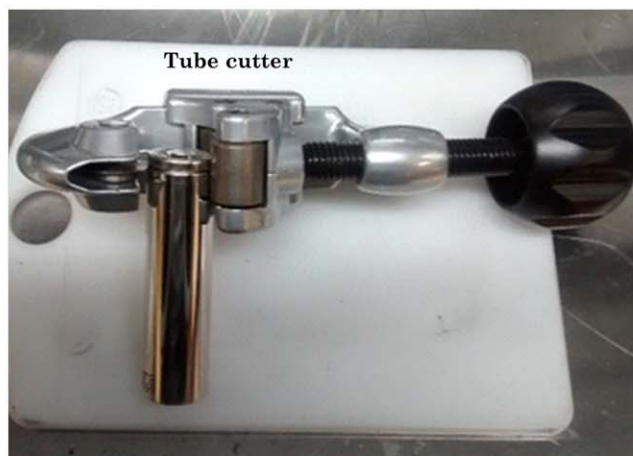
### Appendix A

**A.1. Destructive physical analysis.**—Destructive physical analysis (DPA) provides insights through visual inspection on the physical degradation of the individual components embedded in the Li-ion cell. The procedure involves a sequence of steps aim to determine any abnormality of the cell and preserving the degradation evidence present on each of the cell components. DPA is especially helpful in cases when the cell undergoes, intentionally or unintentionally, into an electrochemical, mechanical and/or thermal abuse scenario. A physical inspection of the abused cell can help to visualize the starting failure zone. Localized root cause becomes significant in forensic analysis of incidents involving Li-ion cells.

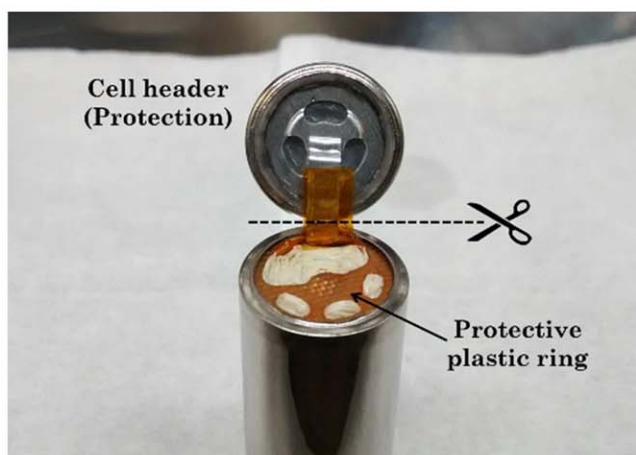
DPA consists of an in-house protocol conducted in an inert Argon-filled glovebox ( $H_2O < 0.5$  ppm,  $O_2 < 0.5$  ppm). The procedure is aimed to be implemented on cylindrical cells. It is recommended to fully discharge the cell prior disassembly when possible. The person conducting the DPA must be familiar with the Li-ion technologies, in particular with architecture of the cylindrical cells. Cells subjected to disassembly may overheat or get internally shorted during the procedure, resulting in an unsafe condition. Additional caution measures must be observed when DPA is conducted on abused cells to reduce the risk of health hazards.



(a)



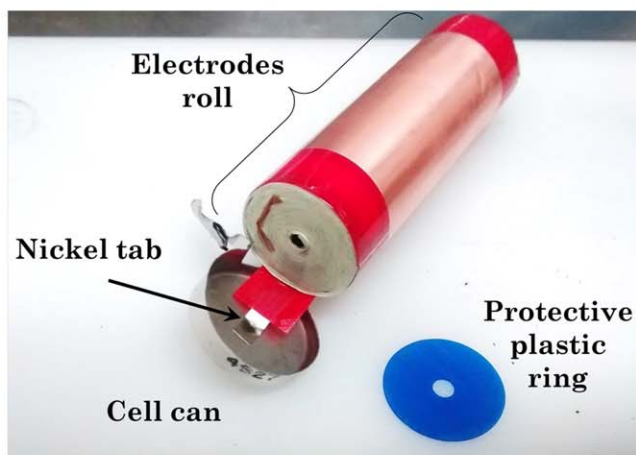
(b)



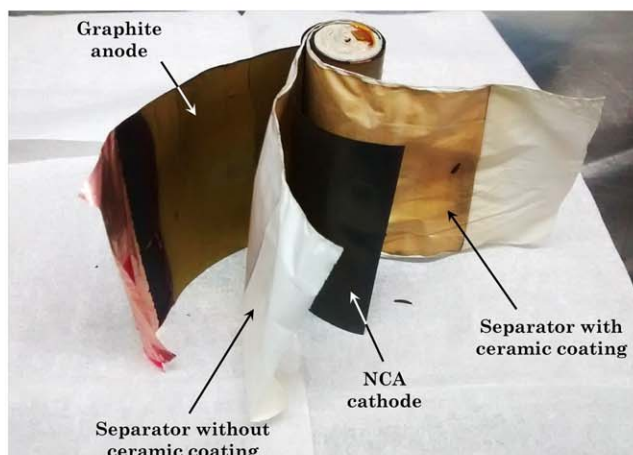
(c)



(d)



(e)



(f)

**Figure A-1.** In-house procedure used to harvest the cell components while preserving the degradation evidence. (a) Step 1: nickel tabs and plastic wrapping removal. (b) Step 2: cell opening. (c) Step 3: cell header removal. (d) Step 4: metallic casing removal. (e) Step 5: jelly roll extraction. (f) Step 8: electrodes/separators split-up.

*Step 1.*—The nickel tabs are removed by prying them with narrow tipped pliers. Then, the thin plastic wrapping, surrounding the cell, is removed by making two small cuts with the scalpel and then peeling the plastic by hand.

*Step 2.*—The cell header is removed using a tube cutter. The adjusting screw is turned to bring the cutting wheel and the cell crimping notch into contact. The cell header is gradually cut by rotating the tool around the clamped notch and tightening the adjusting screw.

**Step 3.**—The thin electrical connection between the cell cap and the rest of the cell is snipped with scissors. Caution must be taken to avoid direct contact between the metallic scissors and the cell can since it can externally short the cell.

**Step 4.**—Starting at the top of the cell where housing is crimped, the protective metal can be removed using a thin-nosed plier and an end-nipper plier by peeling off the metal housing toward the bottom of the cell. The protective plastic located on top of the electrodes is removed.

**Step 5.**—Once the metal housing has been removed to the bottom, the electrical connection located at the bottom of the cell is cut. Then, the blue protective plastic located on the bottom of the jelly roll is removed.

**Step 6.**—If any residual of liquid electrolyte is visible, it is collected in a labeled glass vial. If not liquid electrolyte is found, then, the electrodes are rinsed with isopropyl alcohol (IPA) and the mixture is collected for further composition analysis.

**Step 7.**—The tape holding the electrodes together and the nickel tab placed in between the tape and the copper foil are removed.

**Step 8.**—The two long electrode ribbons and the two separators are unrolled and separated. Take care not to short the electrodes by getting them in direct contact during this process. Pictographically evidence of each electrode and the separator facing it is recommended.

**Step 9.**—The cell components are stored within the inert glovebox in sealing bags. It is recommended to store anode, cathode, separators and the rest of the components in separated bags. By following this procedure, degradation evidence can be preserved in good condition even after one year. If the samples have to be transferred out of the glovebox, then, the sealing bags can be placed under vacuum using a commercial vacuum sealer, and the evidence will not be destroyed.

## ORCID

Daniel Juarez-Robles  <https://orcid.org/0000-0003-2746-5775>  
 Judith A. Jeevarajan  <https://orcid.org/0000-0003-4843-7597>  
 Partha P. Mukherjee  <https://orcid.org/0000-0001-7900-7261>

## References

- S. P. S. Badwal, S. S. Giddey, C. Munnings, A. I. Bhatt, and A. F. Hollenkamp, *Frontiers in Chemistry*, **2** (2014).
- U. S. E. I. Administration, *Annual Energy Outlook 2018 with Projections to 2050* (2018).
- N. Nitta, F. Wu, J. T. Lee, and G. Yushin, *Mater. Today*, **18**, 252 (2015).
- B. Scrosati and J. Garche, *J. Power Sources*, **195**, 2419 (2010).
- J. Gale, P. a. H. M. S. Administration, *Hazardous Materials; Transportation of Lithium Batteries E7-15213*, 44929 (2007), <https://www.federalregister.gov/documents/2007/08/09/E7-15213/hazardous-materials-transportation-of-lithium-batteries>.
- D. Lisbona and T. Snee, *Process Saf Environ*, **89**, 434 (2011).
- C. Chanson and J.-P. Wiaux, *Safety of Lithium-Ion Batteries* (RECHARGE aisbl, Brussels, Belgium) p. 10 (2013).
- B. Jansen, *Crash Investigators Trace UPS Plane Fire to Batteries* (USA Today) Online (2013).
- FAA, *Pack SafeBatteries, lithium*, p. 57, [https://www.faa.gov/hazmat/packsafe/more\\_info/?hazmat=7](https://www.faa.gov/hazmat/packsafe/more_info/?hazmat=7).
- S. Tibken and R. Cheng, *Samsung Answers Burning Note 7 Questions, Vows Better Batteries* (CNET) (2017).
- C. Matyszczyk, *Dell Laptop Explodes Again and Again* (CNET) (2017).
- D. P. S. F. Mario, J. B. Robinson, B. Tjadenm, M. Di Michiel, G. Hinds, D. J. L. Brett, and P. R. Shearing, *Phys. Chem. Chem. Phys.* (2016).
- T. Waldmann et al., *J. Electrochem. Soc.*, **163**, A2149 (2016).
- E. J. Cairns and P. Albertus, *Annual Review of Chemical and Biomolecular Engineering*, **1**, 299 (2010).
- B. Balagopal, C. S. Huang, and M. Chow, "Effect of calendar aging on li ion battery degradation and SOH." *Ilecon 2017—43rd Annual Conference of the IEEE Industrial Electronics Society, Beijing*, 7647 (2017).
- N. Omar, Y. Firouz, H. Gualous, J. Salminen, T. Kallio, J. M. Timmermans, T. Coosemans, P. Van den Bossche, and J. Van Mierlo, *Rechargeable Lithium Batteries: from Fundamentals to Applications*, ed. A. A. Franco p. 263 (2015).
- P. Yuliya, M. B. Heather, F. Armando, L. C. Daniel, W. J. Benjamin, R.-K. Jessica, R. F. Summer, and R. C. Babu, *J. Electrochem. Soc.* (2020).
- A. Iturrondobeitia, F. Aguesse, S. Genies, T. Waldmann, M. Kasper, N. Ghanbari, M. Wohlfahrt-Mehrens, and E. Bekaert, *J. Phys. Chem. C*, **121**, 21865 (2017).
- P. S. Keil, F. Simon, J. Wilhelm, J. Travi, A. Hauser, R. C. Karl, and A. Jossen, *J. Electrochem. Soc.*, **163**, A1872 (2016).
- P. Barai and P. P. Mukherjee, *J. Electrochem. Soc.*, **163**, A1120 (2016).
- T. Waldmann, B.-I. Hogg, and M. Wohlfahrt-Mehrens, *J. Power Sources*, **384**, 107 (2018).
- C. Birkenmaier, B. Bitzer, M. Harzheim, A. Hintennach, and T. Schleid, *J. Electrochem. Soc.*, **162**, A2646 (2015).
- M. Brousse, *Advances in Lithium-Ion Batteries*, ed. W. A. Van Schalkwijk and B. Scrosati (Boston, MA, Springer) p. 393 (2002).
- S. J. An, J. L. Li, C. Daniel, D. Mohanty, S. Nagpure, and D. L. Wood, *Carbon*, **105**, 52 (2016).
- K. Van Havenbergh, S. Turner, K. Driesen, J. S. Bridel, and G. Van Tendeloo, *Energy Technol-Ger.*, **3**, 699 (2015).
- A. Eddahech, O. Briat, and J. M. Vinas, *Energy*, **84**, 542 (2015).
- S. Grolleau, A. Delaille, H. Gualous, P. Gyan, R. Revel, J. Bernard, E. Redondo-Iglesias, J. Peter, and S. Network, *J. Power Sources*, **255**, 450 (2014).
- P. Ramadass, B. Haran, R. White, and B. N. Popov, *J. Power Sources*, **112**, 606 (2002).
- K. Jalkanen, J. Karppinen, L. Skogstrom, T. Laurila, M. Nisula, and K. Vuorilehto, *Appl Energy*, **154**, 160 (2015).
- T. Waldmann, M. Wilka, M. Kasper, M. Fleischhammer, and M. Wohlfahrt-Mehrens, *J. Power Sources*, **262**, 129 (2014).
- S. Zhang, *Journal of Power Sources*, **161**, 1385 (2006).
- L. Somerville, J. Bareno, S. Trask, P. Jennings, A. McGordon, C. Lyness, and I. Bloom, *J. Power Sources*, **335**, 189 (2016).
- C. Fear, D. Juarez-Robles, J. A. Jeevarajan, and P. P. Mukherjee, *J. Electrochem. Soc.*, **165**, A1639 (2018).
- S. Hossain, Y.-K. Kim, Y. Saleh, and R. Loutfy, *J. Power Sources*, **161**, 640 (2006).
- J. Neubauer and A. Pesaran, *J. Power Sources*, **196**, 10351 (2011).
- P.-T. Chen, F.-H. Yang, Z.-T. Cao, J.-M. Jhang, H.-M. Gao, M.-H. Yang, and K. David, *Huang, Batteries & Supercaps*, **2** (2019).
- P. Ramadass, B. Haran, R. White, and B. N. Popov, *J. Power Sources*, **112**, 614 (2002).
- P. Keil and A. Jossen, *J Energy Storage*, **6**, 125 (2016).
- T. M. Bandhauer, S. Garimella, and T. F. Fuller, *J. Electrochem. Soc.*, **158**, R1 (2011).
- H. He, Y. D. Liu, Q. Liu, Z. F. Li, F. Xu, C. Dun, Y. Ren, M. X. Wang, and J. Xie, *J. Electrochem. Soc.*, **160**, A793 (2013).
- J.-F. Li, C.-H. Lin, and K.-C. Chen, *J. Electrochem. Soc.*, **165**, A3634 (2018).
- Q. Yang, J. Xu, B. Cao, D. Xu, X. Li, and B. Wang, *Energy Procedia*, **105**, 2342 (2017).
- B. Koo, J. Yi, D. Lee, C. B. Shin, and S. Park, *J. Electrochem. Soc.*, **165**, A3674 (2018).
- A. Maheshwari, M. Heck, and M. Santarelli, *Electrochim. Acta*, **273**, 335 (2018).
- A. Pfrang, A. Kersys, A. Kriston, D. U. Sauer, C. Rahe, S. Kaebitz, and E. Figgemeier, *J. Power Sources*, **392**, 168 (2018).
- N. Paul, J. Keil, F. M. Kindermann, S. Schebesta, O. Dolotko, M. J. Muehlbauer, L. Kraft, S. V. Erhard, A. Jossen, and R. Gilles, *J Energy Storage*, **17**, 383 (2018).
- M. Hagen, D. Hanselmann, K. Ahlbrecht, R. Maca, D. Gerber, and J. Tubke, *Adv. Energy Mater.*, **5** (2015).
- P. C. o. N. America, *Lithium Ion Batteries (Li-Ion): Cylindrical Series* (Panasonic) 1 (2016).
- D. Aurbach, E. Zinigrad, Y. Cohen, and H. Teller, *Solid State Ionics*, **148**, 405 (2002).
- S. Zhang, K. Xu, and R. Jow, *J. Electrochem. Soc.*, **149**, A1521 (2002).
- I. Bloom, L. K. Walker, J. K. Basco, D. P. Abraham, J. P. Christophersen, and C. D. Ho, *J. Power Sources*, **195**, 877 (2010).
- H. M. Dahn, A. J. Smith, J. C. Burns, D. A. Stevens, and J. R. Dahn, *J. Electrochem. Soc.*, **159**, A1405 (2012).
- K. G. Gallagher, D. W. Dees, A. N. Jansen, D. P. Abraham, and S. H. Kang, *J. Electrochem. Soc.*, **159**, A2029 (2012).
- A. Mandli, A. Kaushik, R. Patil, A. Naha, K. Hariharan, S. M. Kolake, S. Han, and W. Choi, *International Journal of Energy Research*, **43**, 1 (2019).
- D. Juarez-Robles, A. A. Vyas, C. Fear, J. A. Jeevarajan, and P. P. Mukherjee, *J. Electrochem. Soc.*, **167**, 1 (2020).
- P. M. Attia, W. C. Chueh, and S. J. Harris, *J. Electrochem. Soc.*, **167**, 090535 (2020).
- X.-G. Yang, Y. Leng, G. Zhang, S. Ge, and C.-Y. Wang, *J. Power Sources*, **360**, 28 (2017).
- P. Barai, B. Huang, S. J. Dillon, and P. P. Mukherjee, *J. Electrochem. Soc.*, **163**, A3022 (2016).
- A. N. Mistry, K. Smith, and P. P. Mukherjee, *Acs Appl Mater Inter*, **10**, 28644 (2018).

60. A. N. Mistry, H. R. Palle, and P. Mukherjee, *Operando Thermal Signature Probe for Lithium-Ion Batteries*, **114**, 1 (2019).
61. A. Verma, K. Smith, S. Santhanagopalan, D. Abraham, K. Pierre Yao, and P. Mukherjee, *J. Electrochem. Soc.*, **164**, A3380 (2017).
62. P. Maire, A. Evans, H. Kaiser, W. Scheifele, and P. Novak, *J. Electrochem. Soc.*, **155**, A862 (2008).
63. K. Park, J. H. Cho, K. Shanmuganathan, J. Song, J. Peng, M. Gobet, S. Greenbaum, C. J. Ellison, and J. B. Goodenough, *J. Power Sources*, **263**, 52 (2014).
64. B. Gyenes, D. A. Stevens, V. L. Chevrier, and J. R. Dahn, *J. Electrochem. Soc.*, **162**, A278 (2015).
65. P. Barai, K. Smith, C. F. Chen, G. H. Kim, and P. P. Mukherjee, *J. Electrochem. Soc.*, **162**, A1751 (2015).
66. F.-M. Wang, M.-H. Yu, Y.-J. Hsiao, Y. Tsai, B. J. Hwang, Y.-Y. Wang, and C.-C. Wan, *Aging Effects to Solid Electrolyte Interface (SEI) Membrane Formation and the Performance Analysis of Lithium Ion Batteries*, *International Journal of Electrochemical Science*, **6**, 1014 (2011).